Cu/CuO-Doped ZnO Nanocomposites via Solution Combustion Synthesis for Catalytic 4-Nitrophenol Reduction

Buzuayehu Abebe,* Dereje Tsegaye, Chaluma Sori, Ravikumar Chunchana kuppe Renuka Prasad, and H. C. Ananda Murthy*

ACCESS | Metrics & More | Article Recommendations | Supporting Information

ABSTRACT: The synthesis of optoelectrically enhanced nanomaterials should be continuously improved by employing time- and energy-saving techniques. The porous zinc oxide (ZnO) and copper-doped ZnO nanocomposites (NCs) were synthesized by the time- and energy-efficient solution combustion synthesis (SCS) approach. In this SCS approach, once the precursor−surfactant complex ignition point is reached, the reaction starts and ends within a short time without the need for any external energy. The TGA−DTA analysis confirmed that 500 °C was the point at which stable metal oxide was obtained. The doping and heterojunction strategy improved the optoelectric properties of the NCs more than the individual constituents, which then enhanced the materials' charge transfer and optical absorption capabilities. The porosity, nanoscale crystallite size (15−50 nm), and formation of Cu/CuO-ZnO NCs materials were confirmed from the XRD, SEM, and TEM/HRTEM analyses. The obtained d-spacing values of 0.275 and 0.234 nm confirm the formation of ZnO and CuO crystals, respectively. The decrease in photoluminescence intensity for the doped NCs corroborates a reduction in electron−hole recombination. On the Mott−Schottky analysis, the positive slope for ZnO confirms the n-type character, while the negative and positive slopes of the NCs confirm the p- and n-type characters, respectively. A diffusion-controlled type of charge transfer process on the electrode surface was confirmed from the cyclic voltammetric analysis. Thus, the overall analysis shows the applicability of the less expensive and more efficient SCS for several applications, such as catalysis and sensors. To confirm this, an organic catalytic reduction reaction of 4-nitrophenol to 4-aminophenol was tested. Within three and a half minutes, the catalytic reduction result showed the great potential of NCs over ZnO NPs. Thus, the energy- and time-saving SCS approach has a great future outlook as an industrial pollutant catalytic reduction application.
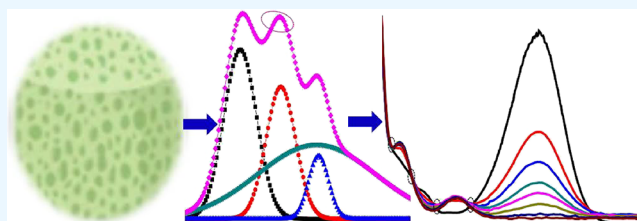
1. INTRODUCTION

The contamination of water due to the release of toxic organic pollutants like 4-nitrophenol leads to carcinogenic and mutagenic effects on human health.[1] 4-Nitrophenol, with its highly stable and soluble properties in water, is used in a variety of industries, including the manufacture of various materials, as an indicator, and as a corrosion inhibitor.[2,3] Thus, the catalytic reduction of 4-nitrophenol to 4-aminophenol (4-AP) has received significant attention.[1,4] The use of nanotechnology, specifically nanomaterials, holds the promise of several applications, such as a clean environment, energy-efficient systems, and human well-being with a less expensive and more efficient process.[5] Zinc oxide (ZnO) is a II−VI semiconductor family material having a wide bandgap of 3.37 eV. It is used in many fields of study, such as catalysis, sensors, and biomedical applications due to its high stability, good crystallinity, and saturation velocity.[6] Copper oxide (CuO), a narrow bandgap p-type semiconductor (1.2−1.8 eV),[7] has high light absorption properties in the visible region. The doping engineering nanotechnology modifies the crucial properties of metal oxide semiconductors, such as optoelectronic, structural,

and charge transfer properties.[8] The doping of copper in the ZnO lattice improves the optoelectric properties better than that of the separate constituents.[9] In addition, forming a p−n junction between CuO and ZnO also creates an electric field greater than their respective constituents and enhances the materials' charge transfer and optical absorption properties.[10]

Solution combustion synthesis (SCS) is one of many simple and energy- and time-efficient methods for improving dopant distribution during the combustion process.[11] SCS follows the decomposition of the precursors in the presence of fuel as a reducing agent to give sol and then gel formation after the heat-assisted solvent removal process. Finally, at the ignition temperature of the complex, the materials begin to combust and quench through the release of gases.[12] The schematic

Scheme 1. Simplified Scheme of the SCS Process[a] Reprinted with permission from ref 19. Copyright 2021 Springer Nature.
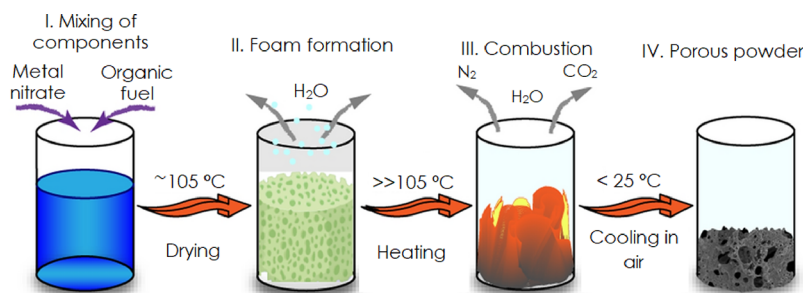
[a]Sol formation by mixing the surfactant, precursors, and fuels; foam formation during dehydration at 105 °C; combustion by gently increasing the temperature up to the PVA/fuel−precursor complex ignition temperature; formation of a porous product by gas evolution.

representation of the solution combustion synthesis approach is depicted in Scheme 1.

According to the authors' literature search, there are many reports about the synthesis of Cu-doped ZnO[13−15] and ZnO/CuO composites[10,16−18] by various methods. However, there is no report on the SCS approach-based synthesis of Cu-doped ZnO/CuO (Cu-ZnO/CuO) NCs for the application of 4-nitrophenol catalytic reduction. As a result, the focus of this study is on the synthesis of Cu-ZnO/CuO NCs using the SCS approach. Crucial analytical techniques such as TGA-DTA, XRD, SEM, TEM/HRTEM/SAED, PL, and CV confirmed the higher porosity and better optoelectric properties of doped nanocomposites compared to single ZnO NPs. Hopefully, this synthesis approach will show good future outlooks for synthesizing porous materials that increase the ion- and mass-transport properties of the materials, which have significance in different applications such as energy devices. In this study, the greater 4-nitrophenol to 4-aminophenol catalytic reduction potential of NCs than ZnO NPs was confirmed.

2. RESULTS AND DISCUSSION

2.1. Characterizations. DTG (TGA/DTA) analysis was used to characterize the thermal stability of ZnO-PVA NCs, which is the temperature required to decompose PVA after capping the synthesized NPs and NCs from aggregation. The PVA decomposition behavior and the temperature at which it decomposes to give pure stabilized ZnO NPs are shown in Figure 1. The total decomposition mass loss was found to be 17% (Figure 1, inset label a). The 3% decomposition is due to the removal of surface or crystal-absorbed water. The 4% is due to the decomposition of the complex formed between PVA and the zinc precursor. The remaining 10% is due to the total decomposition of the PVA polymer. The derivatives of TGA show a DTA spectrum, indicating the two short and broad peaks for water removal and the third intense peak for PVA decomposition. Herein, the total decomposition of PVA to give stable metal oxide was observed at a temperature of 500 °C, and this temperature is used for subsequent characterization analysis. The instability above 500 °C is probably due to the thermal oxidation of the NPs and carbonized residues.[20−22]

The structural and crystallite properties of ZnO NPs, CuO NPs, and Cu-doped NCs synthesized by the SCS approach are characterized by using the XRD pattern. The capping properties of PVA were studied by varying its amount from 0.5 to 2 g (Figure S1a). The smaller crystallite size (greater surface) of 18 nm was obtained for 1 g of PVA (Figure S1b).
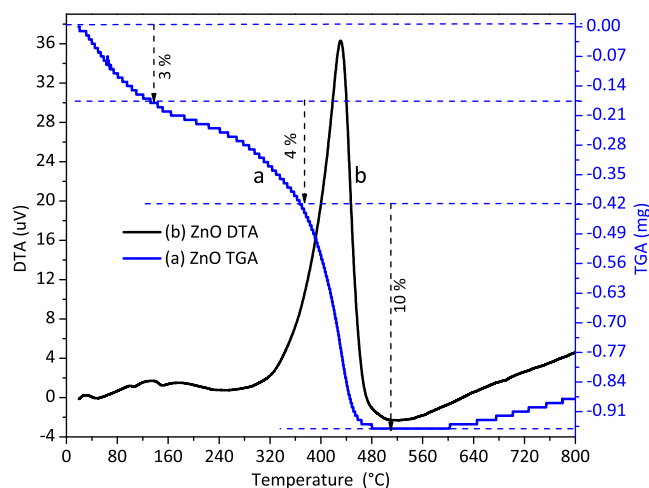

Figure 1. Thermal stability analysis: thermogravimetric (inset label a) and deferential thermal analysis (inset label b) plots of ZnO NPs synthesized using the poly(vinyl alcohol) polymer as a stabilizing agent. The decomposition study was conducted for ZnO-poly (vinyl alcohol) polymer composites before calcination. The optimum decomposition temperature range was determined to be 450−500 °C.

The complex formation between PVA and the precursor (combustion processes) was studied in the presence and absence of urea. The NPs synthesized in the absence of urea (Figure 2a) showed a higher surface area and porosity than those of the NPs/NCs synthesized using urea (Figure S1c,d), indicating the aid of urea in the clumping of NPs/NCs. Of course, the aggregation behavior of urea in water solvent was reported, which then may lead to reduction of the combustion process.[23] The approximate average crystallite sizes of NPs and NCs were calculated using Scherrer's formula.[24] The XRD patterns of Cu-doped ZnO NCs (for 1 and 10% Cu dopants) are studied, as shown in Figure 2, with inset labels d and e. The 10% doped NCs show relatively better crystallite size than 1% NCs. The XRD pattern peak for ZnO and 1% doped ZnO NCs shows hexagonal ZnO wurtzite characteristic peaks at 32°, 34°, 36°, 48°, 57°, 63°, and 68° (JCPDS, file no. 00-036-1451), with the corresponding planes of (100), (002), (101), (102), (110), (103), and (112), respectively.[25]

As shown in Figure 2, the XRD pattern peak for single CuO NPs exhibits a monoclinic phase at 2θ values of 32.4°, 35.6°, 38.7°, 48.8°, 53.5°, 58.3°, and 61.6° (JCPDS, file no. 00-048-1548), with the corresponding planes of (110), (11-1), (200), (20-2), (020), (202), and (11-3), respectively. The absence of a copper-independent peak in the 1% Cu-doped ZnO NCs
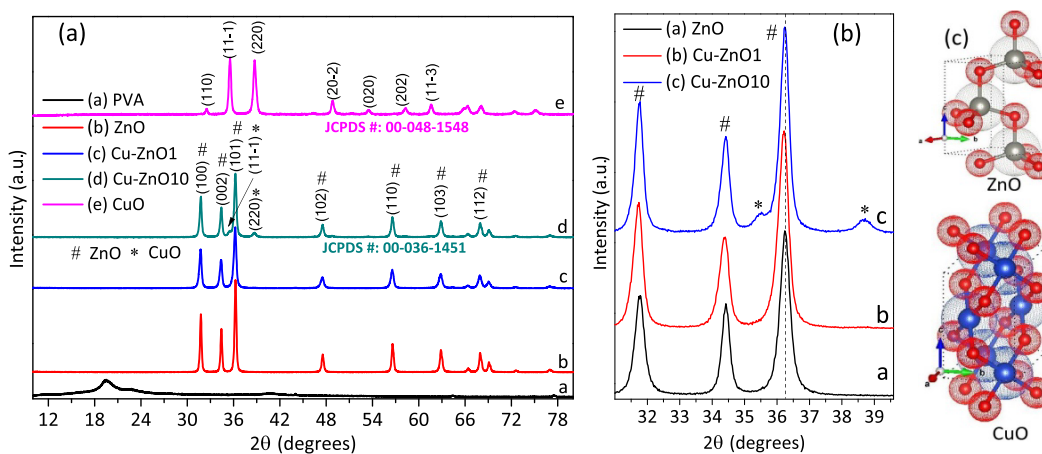
Figure 2. NP and NC structural analysis: (a) XRD patterns of poly(vinyl alcohol), ZnO and CuO NPs, and 1 and 10% Cu-doped ZnO NCs synthesized without urea and (b) magnified view of ZnO NPs and 1 and 10% Cu-doped ZnO NCs. PVA, 1, and 10 in the inset label represent poly(vinyl alcohol) and 1 and 10% copper, respectively. The presence of copper in the ZnO lattice was confirmed by the low-angle shift, and the presence of the CuO peak confirmed the heterojunction for 10% doped NCs. (c) VESTA 3D visualization software was used to create cif data-based structures of stable ZnO and CuO; gray is for Zn, red is for O, and blue is for Cu.
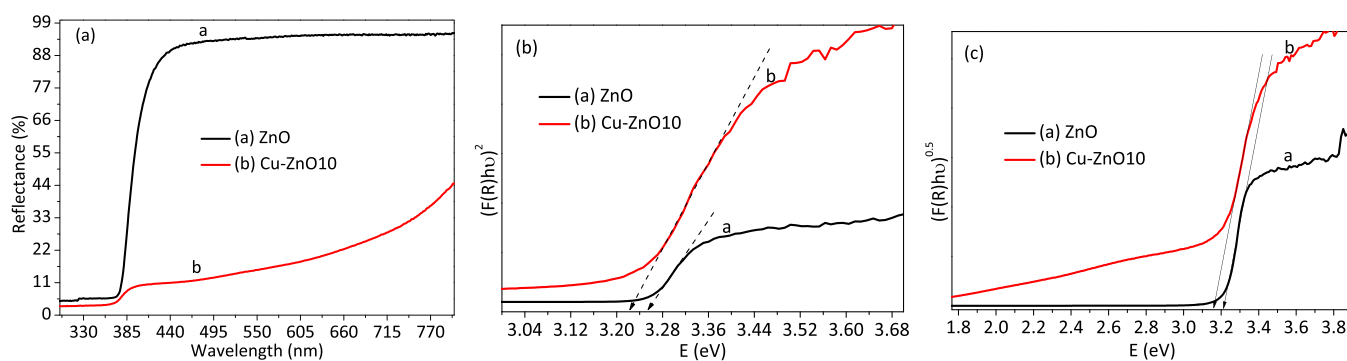

Figure 3. DRS-UV−vis analysis: (a) percent reflectance vs wavelength plots of ZnO NPs and doped NCs and (b, c) direct and indirect Kubelka−Munk function plots of ZnO NPs and doped NCs. The redshift for doped NCs on the Kubelka−Munk function indicates the inclusion of copper in the ZnO lattice. The inset label 10 represents the 10% doped copper.

probably indicates the doping of copper in the ZnO lattice. However, increasing the amount of copper to 10% resulted in the development of two additional monoclinic phases of CuO peaks at 2θ values of 35.5° and 39° with the corresponding planes of (002, 11-1) and (200, 111), respectively.[10,25,26] The slight low-angle shift for doped NCs, especially for 1% doped ZnO NCs, compared to single ZnO NPs confirms the inclusion of copper in the ZnO lattice. Thus, on the 10% doped NCs, both doping and heterojunction took place. The formation of doping and p−n type II heterojunction is important in the photogenerated electron−hole separation (charge transfer) process, which improves the material's photoresponse properties.[10] The development of an independent CuO phase above the optimum dopant percentage (solubility level) was also reported in recent works.[18,25,27] Mahmoud et al. synthesized the Cu-doped ZnO NCs by the sol−gel process. The copper doping up to 4% showed a high-angle peak shift due to substitutional copper doping, with no independent peak for the copper metal or copper oxide. However, increasing the copper percentage to 5% resulted in the appearance of an independent copper oxide peak.[27] Morales-Mendoza et al. synthesized Cu-doped ZnO/CuO NCs with flake-type morphology. The occurrence of an independent monoclinic CuO phase above 6% resulted in the appearance of an independent copper oxide peak and

enhancements in the visible-light absorption range caused by ZnO-CuO heterojunction.[18]

The optical characteristic properties of the ZnO and Cu-doped ZnO NC powders were analyzed by the DRS-UV−vis analytical technique, as shown in Figure 3. The intense and short reflections were observed within the wavelength range of 380−400 nm for ZnO NPs and doped NCs, respectively. The greater reflection properties of ZnO NPs than doped NCs indicate their lower light absorption properties. The greater photoactivity and photon absorption properties of doped NCs (>80%) are probably due to the d−d transition (at a shallow level) that occurred due to the inclusion of copper in the ZnO lattice (Figure 3a). The direct and indirect bandgap energies of NPs and NCs are calculated using the Kubelka−Munk (K−M) function plots[24] by the extrapolation of the linear region toward the x-axis (Figure 3b,c). The direct electron transition occurs in the K−M function when absorbed photoenergy is directly emitted via photogenerated electron−hole recombination. Thus, the crystal momentum (k-vector) value is equal to zero, which means that the maximum VB energy level and minimum CB energy level are equal to zero. However, the k-vector value for the indirect energy bandgap is not equal to zero, indicating that the absorbed energy is not emitted directly.[28] The direct and indirect energy bands obtained for ZnO are 3.26 and 3.22 eV, respectively, whereas the direct and
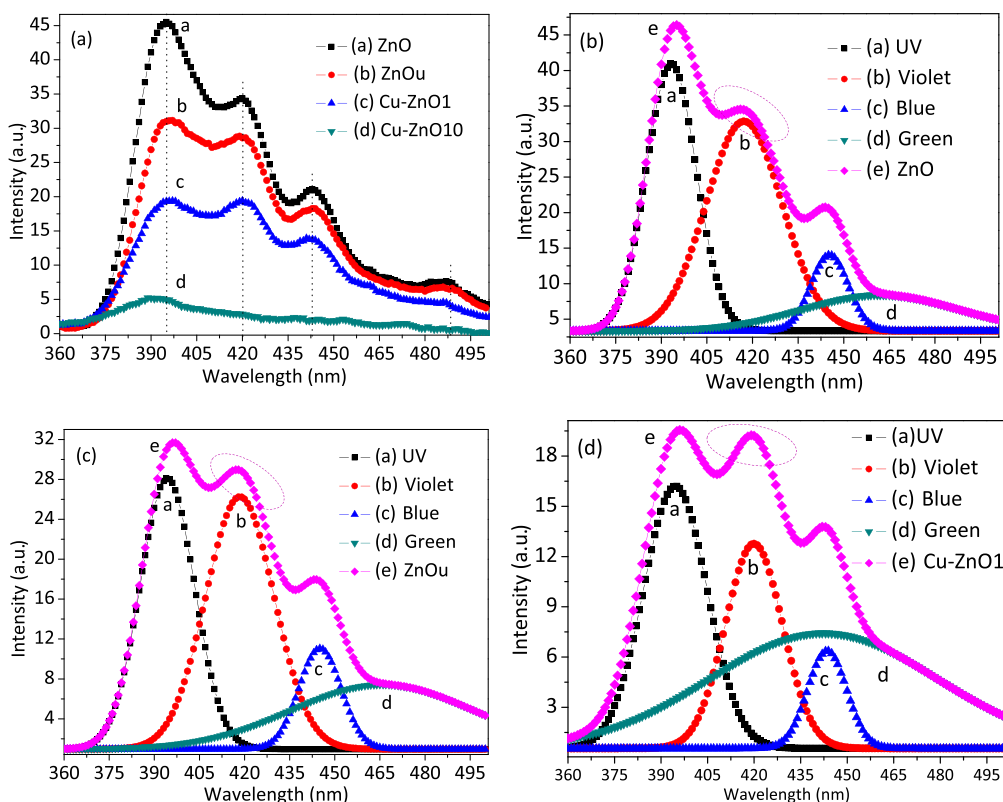
Figure 4. Photoluminescence (PL) analysis of NPs and 10% doped NCs: (a) intensity vs wavelength PL plots of ZnO NPs (synthesized with and without urea) and copper-doped ZnO NCs (1 and 10%) and (b−d) deconvoluted spectra for ZnO, ZnOu, and 1% copper-doped ZnO NCs. This visible peak increment with decreasing UV peak intensity for NCs (1%) confirms the inclusion of copper in the ZnO lattice.
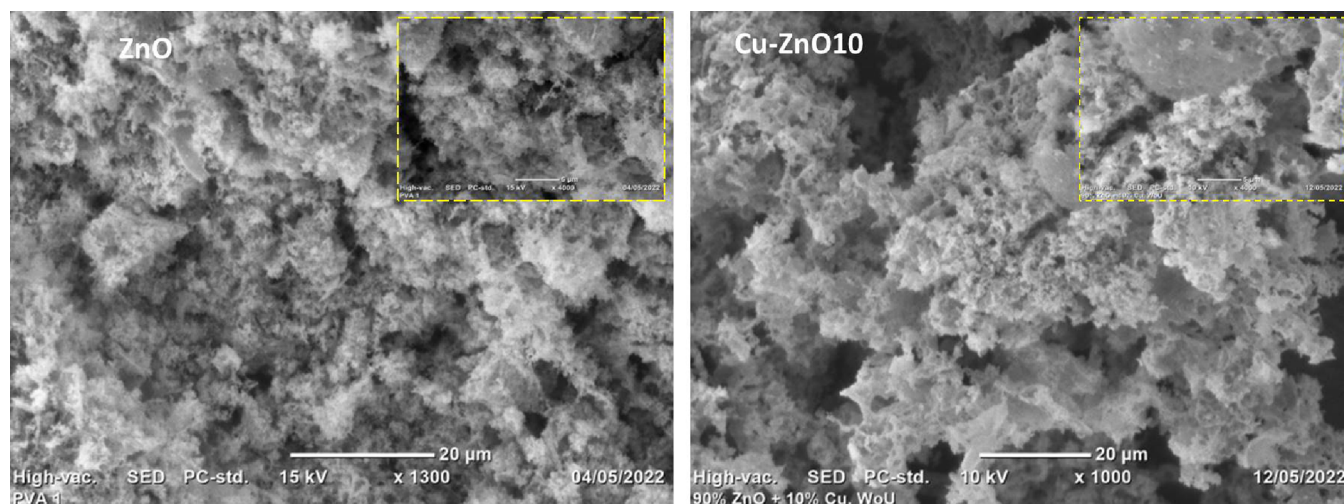

Figure 5. ZnO NP and 10% doped NC scanning electron microscopy (SEM) morphological analysis: The SEM image shows the foam type of porous morphology for 10% Cu-doped ZnO NCs. From close observation, the presence of different pores was observed, which is due to the evolution of gaseous byproducts.

indirect bandgaps for doped ZnO NCs are 3.22 and 3.16 eV, respectively. A bandgap value for doped NCs showed a redshift compared to the ZnO NCs, indicating the creation of additional energy levels due to copper inclusion within the VB and CB of ZnO that stimulate the emission behavior in the visible region, unlike that of ZnO NPs.[29]

By combining the DRS-UV−vis and Mott−Schottky (M−S) analyses, the approximate positions of p-type and n-type semiconductors can be calculated. Figure S2a,b depicts the 1/C^2 versus V reversed sigmoidal M−S plots for single ZnO and

Cu-doped ZnO NCs, respectively. Pure ZnO has a positive slope, and Cu-doped ZnO NCs have both positive and negative slopes. Thus, the positive slope for pure ZnO indicates its n-type character, while the positive and negative slopes for doped NCs indicate their n-type and p-type characters, respectively. The CB flat-band potentials (V_{fb}) were determined by the extrapolation of the linear portion toward the x-axis. The obtained V_{fb} values for pure ZnO and Cu-doped ZnO NCs are −0.66 and −0.62 V (vs Ag/AgCl), respectively. Assuming that the CB edge of n-type semi-
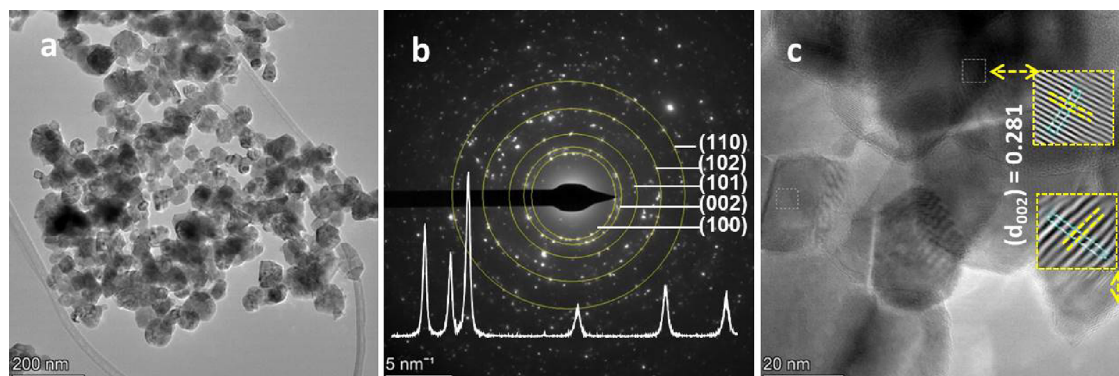
Figure 6. ZnO NPs' transmission electron microscopy (TEM) morphological analysis: (a) In the TEM image, the presence of some pores is observed. (b) In the SAED ring image, the spots on the ring indicate the crystallinity; the inset in panel b is the XRD pattern. (c) In the high-resolution TEM image, the d-spacing analysis shows that all the crystallites are for ZnO NPs.
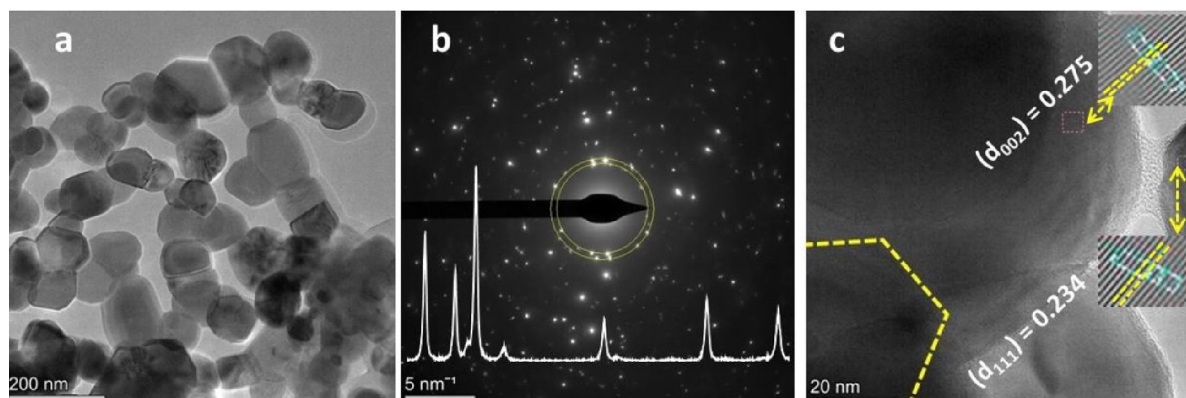

Figure 7. The 10% doped NCs underwent transmission electron microscopy (TEM) morphological analysis: (a) In the TEM image, the presence of pores is observed due to the evolution of gases. (b) In the SAED ring image, the spots on the ring indicate the crystallinity; the inset in panel b is the XRD pattern. (c) In the high-resolution TEM image, the d-spacing analysis shows the presence of both ZnO and CuO NP crystallites.

conductors is 0.1 V lower than the flat-band potentials, the V_{fb} values are −0.56 and −0.52 V (vs NHE).[30] Thus, the VB values of ZnO and doped NCs are 2.66 and 2.64 eV, respectively, based on the DRS-UV−vis (indirect K−M function, ZnO E_g = 3.22 and NC E_g = 3.16) and flat-band potential values (using VB = E_g + CB). The CB flat-band potential of CuO, a p-type character, is 0.58 V (vs Ag/AgCl), which is 0.48 V versus NHE.

The optical properties of the NPs and NCs were further characterized by photoluminescence (PL) spectroscopic techniques, as shown in Figure 4. The PL spectra of ZnO NPs synthesized with and without urea and doped (1 and 10%) NCs show an intense peak at 395 nm, resulting from the near-band edge (NBE) transition that occurred due to the photo-induced electron−hole recombination. In addition, additional peaks occurred in the visible region of 420, 440, and 490 nm as a result of different intrinsic defects (such as deep level emission) and extrinsic defects (such as zinc (Zn_i), oxygen (O_i), oxygen vacancy (V_o), and zinc vacancy (V_{Zn}) and/or chemisorbed O_2, which acts as electron relaxation states[31]). The doped NCs showed a peak intensity reduction compared to the single ZnO, confirming the formation of doping/heterojunction (Schottky contact/metal−semiconductor contact), which diminishes the electron−hole recombination processes.[32] The NP and NC spectrum was further deconvoluted to understand the emission behavior between single ZnO NPs and doped NCs, as shown in Figure 4b−d.

The doped NCs showed a reduction in the UV intensity peak (395 nm) and an increment in the violet (420 nm) peak relative to the UV emission peak (see the pink ellipse mark in Figure 4c,d). This visible peak increment with decreasing UV peak intensity for NCs confirms the inclusion of copper in the ZnO lattice.[33,34]

The morphologies of ZnO NPs and NCs were characterized by SEM and TEM analyses, as shown in Figures 5–7. The SEM images of NPs and NCs synthesized with and without urea in the presence of PVA as a stabilizing agent are shown in Figure S3 (with two different scale bars: the normal image is 20 nm and the inset is 5 nm). The SEM morphology of NPs and NCs synthesized in the presence of urea as a reducing agent and fuel shows a gravelly (less porous) morphology than without urea, indicating that urea is assisting the aggregation. The NPs and NCs synthesized without urea showed better porosity, confirming the formation of a good complex between PVA and the precursor and facilitating the combustion process. In addition, the porous nature of 10% doped NCs (Figure 5b) is better than that of ZnO NPs (Figure 5a) and 1% doped NCs, indicating that the increase in the copper precursor results in an increase in the combustion process. The magnified images for ZnO NPs and 10% doped NCs are given in the respective insets of Figure 5a,b.

The presence of expected elements and their composition were investigated using energy-dispersive X-ray analysis (EDAX), as shown in Figure S4. For ZnO NPs, the presence
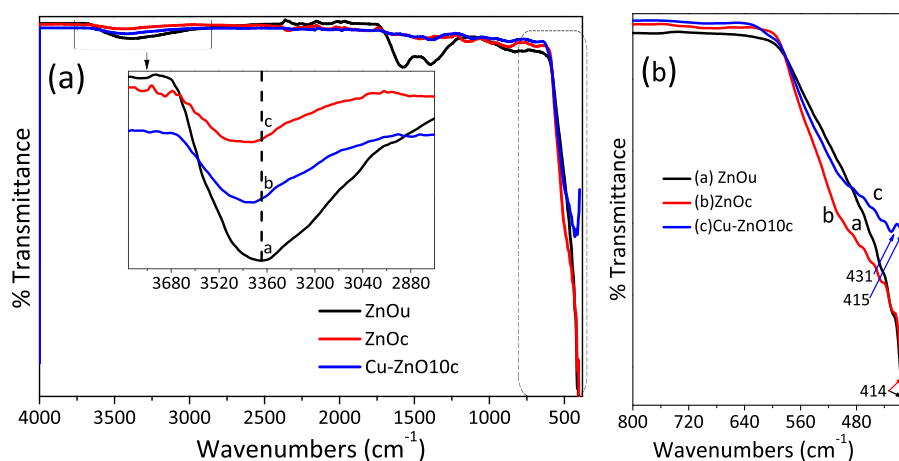
Figure 8. Chemical bonding and functional group analysis: (a) ATR-FTIR spectra of ZnO NPs before and after calcination and calcined 10% doped NCs. The inset in panel (a) is a magnified view of high wavenumber spectra, and panel (b) shows a magnified view of low wavenumber spectra. The band measured between 1570 and 1390 cm^{-1} vanished due to PVA decomposition. The peak for Zn−O/Cu−O detected and the wavenumber shift for the calcined sample show stability enhancement.
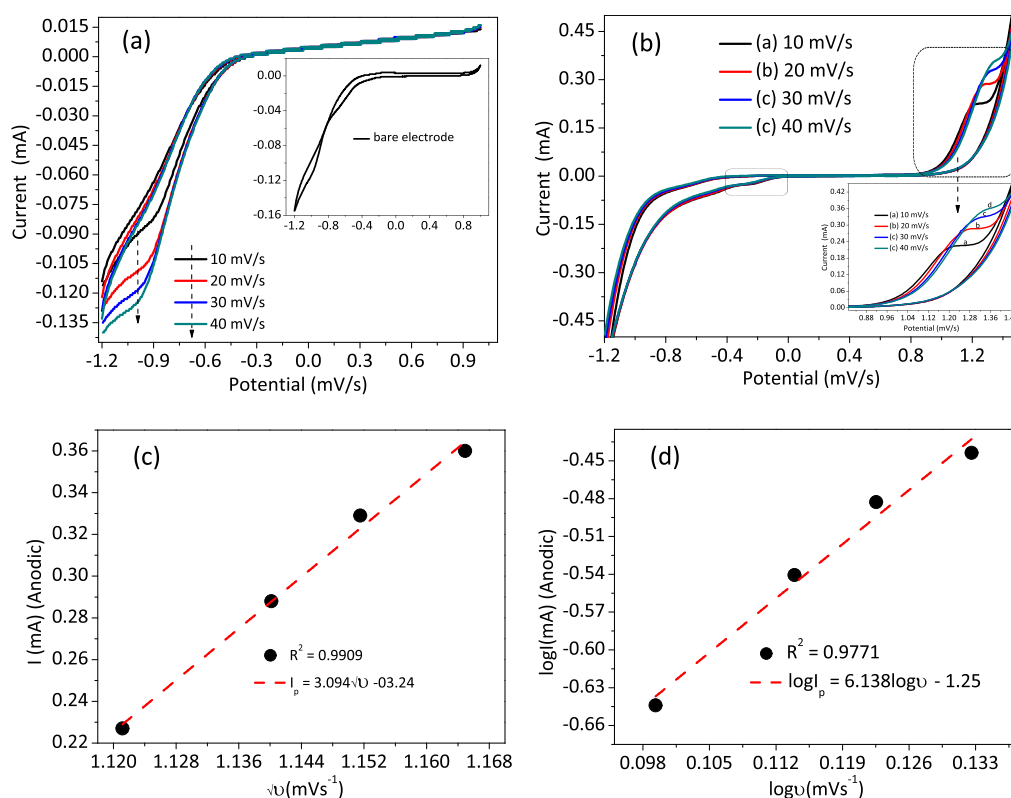

Figure 9. Electrochemical analysis using cyclic voltammetry (CV): (a) CV plots of ZnO NPs. The inset is the fluorine-doped tin oxide (FTO) bare electrode CV plot. (b) CV plots of 10% doped NCs. The inset is the magnified view at higher potential. (c) 10% doped NC anodic peak current and square root linear plot. (d) 10% doped NC log peak current versus log scan rate linear plot. The dominance of the diffusion-controlled charge transfer process is confirmed from the good fitting of the peak current versus square root of the scan rate and log peak current versus log scan rate.

of Zn and O elements at about 1 and 0.5 keV, respectively, was confirmed as a major peak (Figure S4a). For 10% of the NCs, the presence of Zn, Cu, and O at about 1, 0.9, and 0.5 keV, respectively, as a major peak was confirmed (Figure S4b). The occurrence of elemental carbon is probably due to the standard used during analysis. The inset table in Figure S4 shows the compositional analysis results, which are in good agreement with the theoretically calculated weight percentage value.

The detailed morphological characterization was also studied using TEM, HRTEM, and SAED analyses, as shown

in Figures 6 and 7. The TEM image also shows porosity, which is reasonable for the NCs and has occurred during the evolution of the gaseous byproduct. The crystallite sizes for NPs and NCs were found to be in the nanometer range (15−50 nm). Figures 6b and 7b depict the SAED images of ZnO NPs and doped NCs, respectively. The inset plot in the SAED ring is the XRD pattern for ZnO and doped NCs, consistent with the hexagonal wurtzite structure of the SAED ring pattern, specifically for single ZnO NPs. The bright spot observed on the NPs and NCs indicates the crystallinity of the materials.
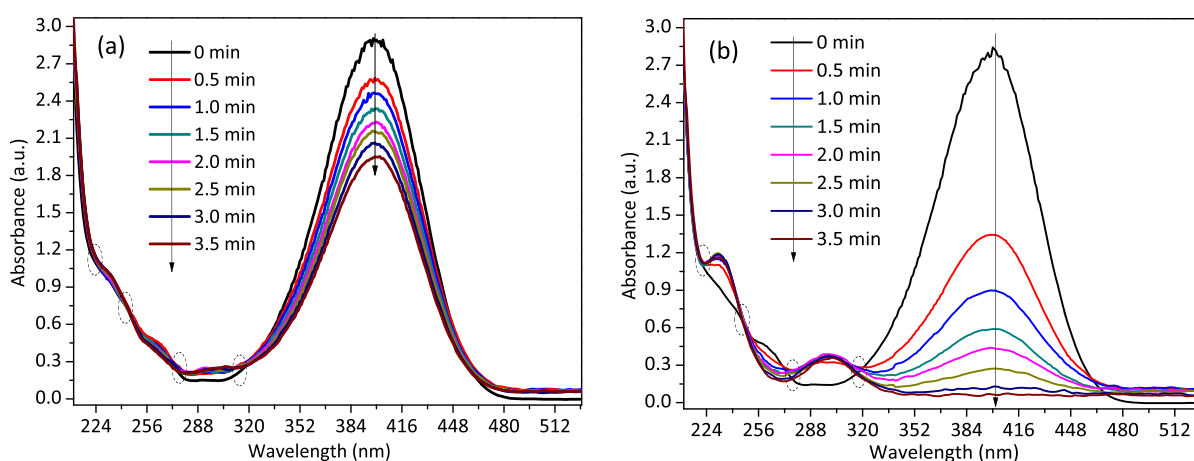
Figure 10. 4-Nitrophenol catalytic reduction plots of (a) ZnO NPs and (b) Cu-doped ZnO NCs: the NCs show complete reduction of 4-nitrophenol to 4-aminophenol within three and a half minutes.

The SAED ring for pure ZnO NPs is clearer than that for NCs, indicating the presence of some structural distortion during the inclusion of the copper dopant in the ZnO lattice. The d-spacing and lattice fringe values (values obtained from the HRTEM image) confirm the actuality of the synthesized NPs and NCs. The calculated d-spacing value for the ZnO NPs was found to be 0.281 nm (Figure 6c), which corresponds to the hexagonal (002) plane of ZnO. The two different d-spacing values for Cu-doped ZnO were found to be 0.275 and 0.234 nm, which match with the (002) plane of ZnO and the cubic (111) plane of CuO NPs, respectively (Figure 7c).[16] The presence of an independent CuO crystallite in the HRTEM image indicates the formation of a localized contact or heterojunction between ZnO and CuO in addition to doping.

The ATR-FTIR technique was used to understand the functional groups, chemical bonding, and composition in the synthesized ZnO NPs (before and after calcination) and Cu-doped NCs (Figure 8). The ATR-FTIR technique works based on the attenuated light created by the evanescent wave between the sample and the internal reflection element interface.[35,36] The broad peak focused at 3380 cm^{-1} is the hydroxyl group's O−H stretching vibration caused by the surface absorption and/or water crystallization (see the magnified inset in Figure 8a). The peak detected at 1400 cm^{-1} is ascribed to the O−C−O symmetric or asymmetric stretching vibration, and the peak at 1575 cm^{-1} is due to the deformation C−OH vibration of the carboxylate group.[37] The relatively intense C−OH deformation and O−C−O stretching vibration peaks observed for ZnO NPs at 1570 and 1390 cm^{-1} before calcination are probably from PVA. These peaks were observed to have disappeared after the calcination of the sample at 500 °C, indicating the total decomposition of PVA, as confirmed on the DTG analysis. The intensity reduction and wavenumber shift were observed after calcination of the sample. The shift to a higher wavenumber (frequency) for the calcined NCs compared to the uncalcined NCs was due to the increased rigidity of the metal−oxygen network as condensation occurred.[38] The peak noticed between 400 and 550 cm^{-1} is attributed to the Zn−O and/or Cu−O vibrational modes (see magnified image in Figure 8b).

The electrochemical tests of ZnO NPs and 10% Cu-doped ZnO NCs were conducted by dissolving and depositing 50 mg of catalysts and *N*-methyl pyrrolidone on the FTO glass substrate (Figure 9). The FTO electrode was first washed and sonicated with acetone for about 20 min. The deposited electrode acts as a working electrode, with the Ag/AgCl saturated electrode as a reference and platinum wire as a counter electrode. Figure 9a, the inset plot, is the cyclic voltammogram of the bare FTO electrode, in which it does not have a visible redox peak, indicating the non-occurrence of a redox reaction. The CV plot of ZnO NCs showed a reduction peak within the −0.9 to −1.0 potential range, probably due to the reduction of Zn ions (Figure 9a). However, the 10% doped NCs show separate reduction peaks for ZnO at the lower potential (−0.3 V) for Zn ion reduction and an oxidation peak at the higher potential (−0.91 to 1.40 V), which is for the oxidation of copper (Figure 9b). The shift in the potential value with an increase in scan rate indicates (i) diffusion of the species through the electrode without adsorption and (ii) the independence of the scan rate on the potential difference.[39] The well-fitting relationship between the peak current and the square root of the scan rate of oxidation peaks indicates the diffusion-controlled charge transfer process on the electrode surface. Potential shifts with an increasing scan rate demonstrate the scan rate's independence from potential and species movement without adsorption. In addition, the closeness between the slope of log peak current versus log scan rate (6.123) and a diffusion-controlled theoretical value of 0.5 confirms the dominance of the diffusion-controlled process.[40]

2.2. 4-Nitrophenol Catalytic Reduction. Figure 10 presents the organic catalytic reduction reaction of 4-nitrophenol to 4-aminophenol (4-AP) in the presence of NaBH$_4$ and the synthesized NP and NC catalysts. 4-Nitrophenol has a maximum wavelength peak at about 317 nm, as shown in Figure S5. The reaction of 4-nitrophenol with NaBH$_4$ produces the 4-nitrophenolate ion, which results in the complete disappearance of the 4-nitrophenol peak at 317 nm and the development of a 4-nitrophenolate ion peak at 400 nm. The reaction of 4-nitrophenol with the catalyst results in the reduction of the 4-nitrophenolate ion and gives 4-AP, with the development of a new peak at a maximum wavelength value of 298 nm. The isotope points (represented by ellipses in Figure 10b) indicate a conversion process that produces no unwanted byproducts.[41] 4-Nitrophenol, 4-nitrophenolate ion, and 4-AP show yellow and deep yellow colors and colorlessness during the reaction process, respectively. The ZnO NPs showed slow catalytic reduction potential on 4-nitrophenol, and the NCs
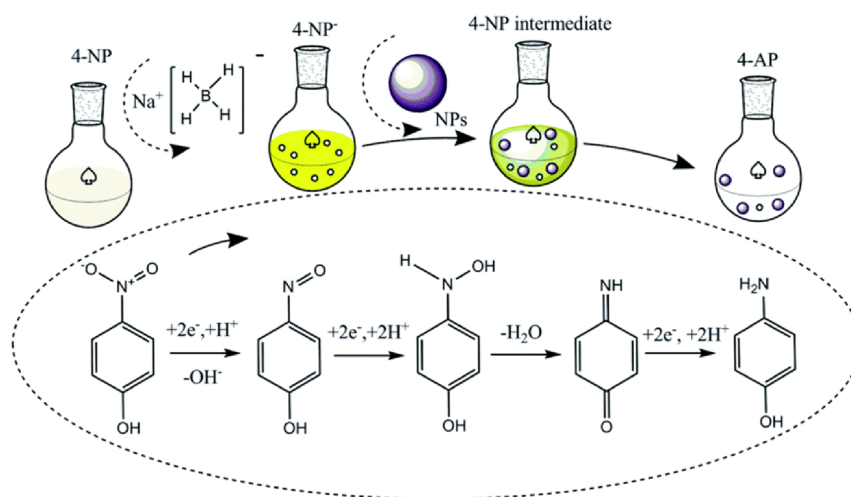
Figure 11. Possible 4-nitrophenol to 4-aminophenol conversion mechanism. During the catalytic reduction process, $NaBH_4$ acts as a H_2 source and the metal nanoparticles as a catalyst. Reprinted with permission from ref 1. Copyright 2022 Royal Society of Chemistry.

showed fast and efficient reduction potential within three and a half minutes, which is probably due to the doping and p−n junction heterojunction effects.[9,10]

The recently reported literature[1,4,42] was used to develop a possible 4-nitrophenol catalytic reduction reaction mechanism to 4-aminophenol (Figure 11). First, when $NaBH_4$ is added to water, a small amount of bubbles forms due to hydrogen generation; this is a reduction reaction between $NaBH_4$ and water. Then, upon addition of the catalyst, it results in the formation of a metal hydride complex. In this catalyst addition stage, more bubbles form, probably due to more hydrogen generation and a more complex formation reaction. The metal hydride complex then gives off electrons and generates active hydrogen on the catalyst surface. Simultaneously, 4-nitrophenol adsorbs on the catalyst hydride complex surface, and hydrogen transfer occurs from the hydride complex to 4-nitrophenol. Kong et al. reported the detailed process of hydrogen absorption, formation of water molecules, and its removal via a sequential hydroxyl dehydration process using mass spectrometry and density functional theory analysis.[42] After the formation of the 4-hydroxylaminophenol transition state, 4-nitrophenol is reduced by active hydrogen to the 4-nitrophenolate ion. Then, the 4-nitrophenol ion peak at 400 nm decreased, and the 4-AP peak at 300 nm appeared over time. The formation of a colorless solution indicates the total conversion of the 4-nitrophenol ion to the 4-AP ion. Finally, 4-AP desorption occurs, which aids in catalyst recycling.

3. CONCLUSIONS

The porous ZnO nanoparticles and Cu/CuO-doped ZnO nanocomposites were successfully synthesized by the solution combustion synthesis approach. The PVA polymer was found to play a vital role in capping the NPs and NCs. At the TGA-DTA-optimized temperature of 500 °C, the PVA polymer was decomposed after its role as a stabilizing agent. The successful inclusion of Cu in the ZnO lattice for 1% was confirmed by the low-angle XRD peak shift. The existence of an independent CuO peak in the XRD pattern and HRTEM image for 10% indicates occurrences of CuO crystals. The porous morphology of NPs and NCs was confirmed from the SEM and TEM images. HRTEM images confirmed the slight d-spacing value differences between the single ZnO crystal and the Cu-doped

ZnO crystal, indicating copper inclusion in the ZnO lattice. The redshift on DR-UV−vis for doped NCs compared to the ZnO NPs showed an improvement in their optical properties. Intensity reduction in PL and n- and p-type characters in the CV Mott−Schottky analysis for doped NCs than ZnO NPs show improvements in the electrical property. As a result, the solution of combustion synthesis-based synthesized doped nanocomposites has promising prospect for catalysis, sensor, and biomedical applications. The copper-doped zinc oxide nanocomposites outperformed ZnO NPs in the reduction of 4-nitrophenol to 4-aminophenol.

4. EXPERIMENTAL SECTION

4.1. Reagents and Chemicals. The reagents and chemicals used are copper(II) nitrate trihydrate ($Cu(NO_3)_2 \cdot 3H_2O$, 99.5%), zinc nitrate ($Zn(NO_3)_2 \cdot 6H_2O$, 99.5%), polyvinyl alcohol ($[-CH_2CHOH-]_n$), urea (CH_4N_2O), and deionized or distilled water.

4.2. Nanoparticle and Nanocomposite Synthesis. The nanoparticles and nanocomposites were synthesized based on the previous studies,[19,20,43] with further improvement using the solution combustion synthesis method. The PVA-polymer-stabilized ZnO NPs were synthesized by dissolving the zinc nitrate ($Zn(NO_3)_2 \cdot 6H_2O$) precursor in the previously dissolved and cooled PVA suspension. The PVA suspension was prepared by dissolving appropriate amounts of PVA in 50 mL of distilled water at about 75 °C with continued stirring for about 20 min.[20] Five different amounts of the polymer (0.1−2 g) were taken at a fixed amount of zinc precursor and optimized. The zinc precursor−PVA sol complex[44] was then further dehydrated by heating to approximately 110 °C. Continually increasing the gel temperature has consequences for the combustion of the complex formed between the precursor and PVA, resulting in the porous, spongy type of the finished product. Finally, the combusted material was softly crushed to powder and calcined at the TGA-DTA-optimized temperature of 500 °C for 3 h. The steps for the synthesis of ZnO NPs in the presence of urea are similar, with the exception of the dropwise addition of urea solution from the burette (0.16 M), which forms a 1:1 ratio with the precursor. The synthesis of ZnO NPs in the absence of PVA and urea also follows the same above-mentioned procedure, excluding the

first PVA dissolving step. In addition, single CuO NPs and Cu-doped ZnO (1 and 10%) use an appropriate amount of copper dopant and zinc host precursor and follow the same above-mentioned procedures.

4.3. Catalytic 4-Nitrophenol Reduction Procedure. The potential of NPs and NCs for 4-nitrophenol to 4-AP reduction was investigated using sodium borohydride (NaBH$_4$) as a reducing agent, as previously reported[45] with minor modifications. In detail, 1.10 mL of 0.01 M 4-NP was dissolved in 0.38 g/100 mL (0.1 M) of excess NaBH$_4$ to give a deep yellow color. The mixture was then mixed with 10 mg of the catalyst, and the 4-nitrophenol reduction to 4-AP was monitored using a UV−vis spectrophotometer (P9 UV/Visible double-beam spectrophotometer).

4.4. Characterizations. The thermal decomposition behavior of PVA-ZnO was investigated using a thermogravimetric-differential thermal analyzer (TGA-DTA, DTG-60H). The X-ray diffraction method (XRD, Shimadzu, XRD-7000) was used to study the catalyst crystallite size, crystallinity, and structure. Diffuse reflectance ultraviolet−visible (DRS-UV−vis; Shimadzu, UV-2600) spectroscopy was used to study the optical property. Further optical and electrical properties of the materials were characterized by photoluminescence spectroscopy at the excitation wavelength of 325 nm (PL, eclipse fluorescence spectrophotometer, Agilent). Scanning electron microscopy (SEM, JCM-6000Plus), transmission electron microscopy (TEM), selected-area electron diffraction (SAED), and high-resolution TEM (HRTEM) (JEOL TEM 2100 HRTEM) showed the porosity, crystallinity, and morphology of the materials. The chemical bonding properties and compositional study were characterized by attenuated total reflectance-Fourier transform infrared spectroscopy (ATR-FTIR, Nicolet iS50 FTIR). The electrochemical tests were conducted using the cyclic voltammetry technique (CH 660E workstation). The Mott−Schottky analysis was accomplished using a 0.1 M Na$_2$SO$_4$ solution as an electrolyte at 800 Hz frequency, sweeping the potential in the range of +1.0 to −1.2 V. The electrochemical test was conducted in a three-electrode system with an FTO-loaded catalyst, silver−silver chloride, and platinum electrodes as the working, reference, and counter electrodes, respectively.

■ ASSOCIATED CONTENT

ⓈⒾ Supporting Information

The Supporting Information is available free of charge at https://pubs.acs.org/doi/10.1021/acsomega.3c00141.

> XRD pattern structural analysis of PVA, ZnO, CuO NPs, and Cu-doped ZnO NCs; Mott−Schottky plots of ZnO NPs and 10% NCs; SEM morphological analysis images of ZnO NPs and NCs; EDAX compositional results of ZnO NPs and NCs; conversion of 4-nitrophenol to 4-nitrophenolate ions (PDF)

■ AUTHOR INFORMATION

Corresponding Authors

Buzuayehu Abebe − *Department of Applied Chemistry, School of Applied Natural Science, Adama Science and Technology University, Adama 1888, Ethiopia;* ⓞ orcid.org/0000-0001-6076-4932; Phone: +251910418009; Email: buzea8@gmail.com

H. C. Ananda Murthy − *Department of Applied Chemistry, School of Applied Natural Science, Adama Science and*

Technology University, Adama 1888, Ethiopia; Department of Prosthodontics, Saveetha Dental College & Hospital, Saveetha Institute of Medical and Technical Science (SIMATS), Saveetha University, Chennai 600077 Tamil Nadu, India; ⓞ orcid.org/0000-0002-2361-086X; Phone: +251988683640; Email: anandkps350@gmail.com

Authors

Dereje Tsegaye − *Department of Applied Chemistry, School of Applied Natural Science, Adama Science and Technology University, Adama 1888, Ethiopia*

Chaluma Sori − *Department of Applied Chemistry, School of Applied Natural Science, Adama Science and Technology University, Adama 1888, Ethiopia*

Ravikumar Chunchana kuppe Renuka Prasad − *Research Centre, Department of Science, East-West Institute of Technology, Bangalore 560091, India;* ⓞ orcid.org/0000-0002-4692-444X

Complete contact information is available at:
https://pubs.acs.org/10.1021/acsomega.3c00141

Author Contributions

Writing of the original draft and investigation by B.A. Review and editing by D.T. and H.C.A.M. Resources by C.S. Sample analysis by R.C.k.R.P. All authors read in detail and approved the final manuscript.

Notes

The authors declare no competing financial interest.

■ ACKNOWLEDGMENTS

■ REFERENCES

(1) Mejía, Y. R.; Reddy Bogireddy, N. K. Reduction of 4-Nitrophenol Using Green-Fabricated Metal Nanoparticles. *RSC Adv.* **2022**, *12*, 18661−18675.

(2) Chen, Y.; Feng, L.; Sadeghzadeh, S. M. Reduction of 4-Nitrophenol and 2-Nitroaniline Using Immobilized CoMn 2 O 4 NPs on Lignin Supported on FPS. *RSC Adv.* **2020**, *10*, 19553−19561.

(3) Bagheri, M.; Melillo, A.; Ferrer, B.; Masoomi, M. Y.; Garcia, H. Quasi-HKUST Prepared via Postsynthetic Defect Engineering for Highly Improved Catalytic Conversion of 4-Nitrophenol. *ACS Appl. Mater. Interfaces* **2022**, *14*, 978−989.

(4) Wang, Z.; Su, R.; Wang, D.; Shi, J.; Wang, J.-X.; Pu, Y.; Chen, J.-F. Sulfurized Graphene as Efficient Metal-Free Catalysts for Reduction of 4-Nitrophenol to 4-Aminophenol. *Ind. Eng. Chem. Res.* **2017**, *56*, 13610−13617.

(5) Jassby, D.; Cath, T. Y.; Buisson, H. The Role of Nanotechnology in Industrial Water Treatment. *Nat. Nanotechnol.* **2018**, *13*, 670−672.

(6) Jabbar, I.; Zaman, Y.; Althubeiti, K.; Al Otaibi, S.; Ishaque, M. Z.; Rahman, N.; Sohail, M.; Khan, A.; Ullah, A.; Del Rosso, T.; Zaman, Q.; Khan, R.; Khan, A. Diluted Magnetic Semiconductor Properties in TM Doped ZnO Nanoparticles. *RSC Adv.* **2022**, *12*, 13456−13463.

(7) Haghparas, Z.; Kordrostami, Z.; Sorouri, M.; Rajabzadeh, M.; Khalifeh, R. Highly Sensitive Non-Enzymatic Electrochemical Glucose Sensor Based on Dumbbell-Shaped Double-Shelled Hollow Nanoporous CuO/ZnO Microstructures. *Sci. Rep.* **2021**, *11*, 344.

(8) Samriti; Rajput, V.; Gupta, R. K.; Prakash, J. Engineering Metal Oxide Semiconductor Nanostructures for Enhanced Charge Transfer: Fundamentals and Emerging SERS Applications. *J. Mater. Chem. C* **2021**, *10*, 73−95.

(9) Abebe, B.; Murthy, H. C. A. Insights into ZnO-Based Doped Porous Nanocrystal Frameworks. *RSC Adv.* **2022**, *12*, 5816−5833.

(10) Costas, A.; Florica, C.; Preda, N.; Besleaga, C.; Kuncser, A.; Enculescu, I. Self-Connected CuO−ZnO Radial Core−Shell Heterojunction Nanowire Arrays Grown on Interdigitated Electrodes for Visible-Light Photodetectors. *Sci. Rep.* **2022**, *12*, 6834.

(11) Deganello, F.; Tyagi, A. K. Solution Combustion Synthesis, Energy and Environment: Best Parameters for Better Materials. *Prog. Cryst. Growth Charact. Mater.* **2018**, *64*, 23−61.

(12) Nersisyan, H. H.; Lee, J. H.; Ding, J.-R.; Kim, K.-S.; Manukyan, K. V.; Mukasyan, A. S. Combustion Synthesis of Zero-, One-, Two- and Three-Dimensional Nanostructures: Current Trends and Future Perspectives. *Prog. Energy Combust. Sci.* **2017**, *63*, 79−118.

(13) Sivakumar, S.; Robinson, Y.; Mala, N. A. Studies on Photocatalytic Performance and Supercapacitor Applications of Undoped and Cu-Doped ZnO Nanoparticles. *Appl. Surf. Sci. Adv.* **2022**, *12*, No. 100344.

(14) Brahma, S.; Yeh, Y.-W.; Huang, J.-L.; Liu, C.-P. Cu-Doped p-Type ZnO Nanostructures as Unique Acetone Sensor at Room Temperature (~25 °C). *Appl. Surf. Sci.* **2021**, *564*, No. 150351.

(15) Xu, L.; Xian, F.; Zheng, G.; Lai, M. Realization of Strong Violet and Blue Emissions from ZnO Thin Films by Incorporation of Cu Ions. *Mater. Res. Bull.* **2018**, *99*, 144−151.

(16) Nadargi, D. Y.; Tamboli, M. S.; Patil, S. S.; Dateer, R. B.; Mulla, I. S.; Choi, H.; Suryavanshi, S. S. Microwave-Epoxide-Assisted Hydrothermal Synthesis of the CuO/ZnO Heterojunction: A Highly Versatile Route to Develop H 2 S Gas Sensors. *ACS Omega* **2020**, *5*, 8587−8595.

(17) Bekru, A. G.; Tufa, L. T.; Zelekew, O. A.; Goddati, M.; Lee, J.; Sabir, F. K. Green Synthesis of a CuO−ZnO Nanocomposite for Efficient Photodegradation of Methylene Blue and Reduction of 4-Nitrophenol. *ACS Omega* **2022**, *7*, 30908−30919.

(18) Morales-Mendoza, J. E.; Paraguay-Delgado, F. Widening UV−Vis Absorption Band by Cu Doped ZnO and ZnO/CuO Composite. *Mater. Lett.* **2021**, *291*, No. 129494.

(19) Khort, A.; Hedberg, J.; Mei, N.; Romanovski, V.; Blomberg, E.; Odnevall, I. Corrosion and Transformation of Solution Combustion Synthesized Co, Ni and CoNi Nanoparticles in Synthetic Freshwater with and without Natural Organic Matter. *Sci. Rep.* **2021**, *11*, 7860.

(20) Liu, B.; You, Y.; Zhang, H.; Wu, H.; Jin, J.; Liu, H. Synthesis of ZnO Nano-Powders via a Novel PVA-Assisted Freeze-Drying Process. *RSC Adv.* **2016**, *6*, 110349−110355.

(21) Budrugeac, P. Kinetics of the Complex Process of Thermo-Oxidative Degradation of Poly(Vinyl Alcohol). *J. Therm. Anal. Calorim.* **2008**, *92*, 291−296.

(22) Yang, H.; Xu, S.; Jiang, L.; Dan, Y. Thermal Decomposition Behavior of Poly (Vinyl Alcohol) with Different Hydroxyl Content. *J. Macromol. Sci. Part B* **2012**, *51*, 464−480.

(23) Atahar, A.; Mafy, N. N.; Rahman, M. M.; Mollah, M. Y. A.; Susan, M. A. B. H. Aggregation of Urea in Water: Dynamic Light Scattering Analyses. *J. Mol. Liq.* **2019**, *294*, No. 111612.

(24) Abebe, B.; Zereffa, E. A.; Murthy, H. C. A. Synthesis of Poly(Vinyl Alcohol)-Aided ZnO/Mn 2 O 3 Nanocomposites for Acid Orange-8 Dye Degradation: Mechanism and Antibacterial Activity. *ACS Omega* **2021**, *6*, 954−964.

(25) Paraguay-Delgado, F.; Hermida-Montero, L. A.; Morales-Mendoza, J. E.; Durán-Barradas, Z.; Mtz-Enriquez, A. I.; Pariona, N. Photocatalytic Properties of Cu-Containing ZnO Nanoparticles and Their Antifungal Activity against Agriculture-Pathogenic Fungus. *RSC Adv.* **2022**, *12*, 9898−9908.

(26) Chen, M.; Ding, Y.; Gao, Y.; Zhu, X.; Wang, P.; Shi, Z.; Liu, Q. N,N′-Di-Caboxy Methyl Perylene Diimide (PDI) Functionalized CuO Nanocomposites with Enhanced Peroxidase-like Activity and Their Application in Visual Biosensing of H 2 O 2 and Glucose. *RSC Adv.* **2017**, *7*, 25220−25228.

(27) Mahmoud, A.; Echabaane, M.; Omri, K.; Boudon, J.; Saviot, L.; Millot, N.; Chaabane, R. B. Cu-Doped ZnO Nanoparticles for Non-Enzymatic Glucose Sensing. *Molecules* **2021**, *26*, 929.

(28) Schneider, K. Optical Properties and Electronic Structure of V2O5, V2O3 and VO2. *J. Mater. Sci.: Mater. Electron.* **2020**, *31*, 10478−10488.

(29) Thabit, H. A.; Kabir, N. A.; Ismail, A. K.; Alraddadi, S.; Bafaqeer, A.; Saleh, M. A. Development of Ag-Doped ZnO Thin Films and Thermoluminescence (TLD) Characteristics for Radiation Technology. *Nanomaterials* **2022**, *12*, 3068.

(30) Zheng, J.; Lei, Z. Incorporation of CoO Nanoparticles in 3D Marigold Flower-like Hierarchical Architecture MnCo2O4 for Highly Boosting Solar Light Photo-Oxidation and Reduction Ability. *Appl. Catal., B* **2018**, *237*, 1−8.

(31) Ma, Y.; Choi, T.-W.; Cheung, S. H.; Cheng, Y.; Xu, X.; Xie, Y.-M.; Li, H.-W.; Li, M.; Luo, H.; Zhang, W.; So, S. K.; Chen, S.; Tsang, S.-W. Charge Transfer-Induced Photoluminescence in ZnO Nanoparticles. *Nanoscale* **2019**, *11*, 8736−8743.

(32) Alharthi, F. A.; Alghamdi, A. A.; Al-Zaqri, N.; Alanazi, H. S.; Alsyahi, A. A.; El Marghany, A.; Ahmad, N. Facile One-Pot Green Synthesis of Ag−ZnO Nanocomposites Using Potato Peeland Their Ag Concentration Dependent Photocatalytic Properties. *Sci. Rep.* **2020**, *10*, 20229.

(33) Ji, H.; Cai, C.; Zhou, S.; Liu, W. Structure, Photoluminescence, and Magnetic Properties of Co-Doped ZnO Nanoparticles. *J. Mater. Sci.: Mater. Electron.* **2018**, *29*, 12917−12926.

(34) Mahroug, A.; Boudjadar, S.; Hamrit, S.; Guerbous, L. Structural, Morphological and Optical Properties of Undoped and Co-Doped ZnO Thin Films Prepared by Sol−Gel Process. *J. Mater. Sci.: Mater. Electron.* **2014**, *25*, 4967−4974.

(35) Pouran, H.; Perez Colodrero, R.; Wu, S.; Hix, G.; Zakharova, J.; Zhang, H. Assessment of ATR-FTIR Spectroscopy with Multivariate Analysis to Investigate the Binding Mechanisms of Ag and TiO 2 Nanoparticles to Chelex-100 or Metsorb for the DGT Technique. *Anal. Methods* **2020**, *12*, 959−969.

(36) Liu, G.-L.; Kazarian, S. G. Recent Advances and Applications to Cultural Heritage Using ATR-FTIR Spectroscopy and ATR-FTIR Spectroscopic Imaging. *Analyst* **2022**, *147*, 1777−1797.

(37) Sharwani, A. A.; Narayanan, K. B.; Khan, M. E.; Han, S. S. Photocatalytic Degradation Activity of Goji Berry Extract Synthesized Silver-Loaded Mesoporous Zinc Oxide (Ag@ZnO) Nanocomposites under Simulated Solar Light Irradiation. *Sci. Rep.* **2022**, *12*, 10017.

(38) Lan, L.; Gnappi, G.; Montenero, A. Infrared Study of EPOXS-TEOS-TPOT Gels. *J. Mater. Sci.* **1993**, *28*, 2119−2123.

(39) Haque, M.; Fouad, H.; Seo, H.-K.; Othman, A. Y.; Kulkarni, A.; Ansari, Z. A. Investigation of Mn Doped ZnO Nanoparticles Towards Ascertaining Myocardial Infarction Through an Electrochemical Detection of Myoglobin. *IEEE Access* **2020**, *8*, 164678−164692.

(40) Thomas, D.; Rasheed, Z.; Jagan, J. S.; Kumar, K. G. Study of Kinetic Parameters and Development of a Voltammetric Sensor for the Determination of Butylated Hydroxyanisole (BHA) in Oil Samples. *J. Food Sci. Technol.* **2015**, *52*, 6719−6726.

(41) Mei, Y.; Lu, Y.; Polzer, F.; Ballauff, M.; Drechsler, M. Catalytic Activity of Palladium Nanoparticles Encapsulated in Spherical Polyelectrolyte Brushes and Core−Shell Microgels. *Chem. Mater.* **2007**, *19*, 1062−1069.

(42) Kong, X.; Zhu, H.; Chen, C.; Huang, G.; Chen, Q. Insights into the Reduction of 4-Nitrophenol to 4-Aminophenol on Catalysts. *Chem. Phys. Lett.* **2017**, *684*, 148−152.

(43) Gao, Y.; Meng, F.; Li, X.; Wen, J. Z.; Li, Z. Factors Controlling Nanosized Ni−Al 2 O 3 Catalysts Synthesized by Solution Combustion for Slurry-Phase CO Methanation: The Ratio of Reducing Valences to Oxidizing Valences in Redox Systems. *Catal. Sci. Technol.* **2016**, *6*, 7800−7811.

(44) Zhang, J.; Guo, Q.; Liu, Y.; Cheng, Y. Preparation and Characterization of Fe 2 O 3 /Al 2 O 3 Using the Solution Combustion Approach for Chemical Looping Combustion. *Ind. Eng. Chem. Res.* **2012**, *51*, 12773−12781.

(45) Ali, H. M.; Ibrahim, S. M.; Abo Zeid, E. F.; Al-Hossainy, A. F.; El-Aal, M. A. A Comparative Study of Cu-Anchored 0D and 1D ZnO Nanostructures for the Reduction of Organic Pollutants in Water. *RSC Adv.* **2022**, *12*, 16496−16509.